

A Polynomial Framework for Design of Drag Reducing Periodic Two-dimensional Textured Surfaces

Shabnam Raayai-Ardakani*

Rowland Institute, Harvard University, 100 Edwin H. Land Blvd., Cambridge, 02142, MA, USA

Abstract

Periodic and symmetric two-dimensional textures with various cross-sectional profiles have been employed to improve and optimize the physical response of the surfaces such as drag force, superhydrophobicity, and adhesion. While the effect of the height and spacing of the textures have been extensively studied, the effect of the shape of the textures has only been considered in qualitative manners. Here, a polynomial framework is proposed to mathematically define the cross-sectional profiles of the textures and offer a quantitative measure for comparing the physical response of the textured surfaces with various cross-sectional profiles. As a case study, textured surfaces designed with this framework are tested for their hydrodynamic frictional response in the cylindrical Couette flow regime in Taylor- Couette flows. With the reduction in torque as the objective, experimental and numerical results confirm that textures with height-to-half-spacing of lower and equal to unity with concave profiles offer a lower torque compared to both smooth surfaces and triangular textures. In addition, across multiple polynomial orders, textures defined by second order polynomials offer a wide range of responses, eliminating the need for considering polynomials of higher orders and complexity. While the case study here is focused on the laminar flow regime and the frictional torque, the same type of analysis can be applied to other surface properties and physical responses as well.

Keywords: Textured Surfaces, Riblets, Taylor-Couette Flows, Drag Reduction

Introduction

Textures are well documented for their ability to alter and regulate physical response of surfaces, both in the natural and engineering settings; Drag reducing effect of ribs on the denticles of fast swimming shark species [1, 2, 3] as well as bio-inspired riblet-covered surfaces [4, 5, 6, 7, 8, 9, 10, 11, 12, 13, 14, 15, 16, 17, 18], super-hydrophobicity, super-repellency, and self cleaning of *Colocasia esculenta*, *Euphorbia myrsinites*, *Nelumbo nucifera* (Lotus), and *Salvinia* leaves, packed with convex papillose cells which are covered by three-dimensional wax crystal [19, 20, 21, 22, 23, 24], slippery and insect trapping mechanism of the concave textures on the rim (peristome) of *Nepenthes* pitcher plants [25, 26, 27, 28], which can also act as superior fog harvesters [29], as well as excellent adhesion of textures on the feet of gecko and some arthropods [30, 31, 24] and the textured gecko-inspired engineered adhesives [32, 33, 34, 35, 36] are but a few examples.

Textures come in random and ordered configurations, and the characteristics of the profiles and patterns are described with a variety of naming conventions. Terms such as roughness, waviness, and lay [37] in manufacturing, dimples and seams in sports [38, 39], or wrinkles, dimples, and creases in patterns formed with soft materials [40, 41, 42] are a few of the

words commonly used to describe the corresponding topographies. In dealing with random roughness under flow conditions, additional characteristics, such as the roughness topography, local peak-to-trough heights, max peak-to-trough height, or sand grain roughness measures are also considered [43].

One group of idealized and ordered engineering textures are two-dimensional (2D) textures; these are simplified models of natural rib-like textures (shark skin, butterfly wings, rice leaves), and have been widely considered for the purposes of drag reduction [44] and anisotropic surface responses [45, 46]. Such 2D ordered textures are comprised of a unit element of texture that is symmetric and repeated in a periodic pattern (Fig. 1(a)) and unit elements ranging from triangular (also known as V-groove or saw-tooth) [8, 4, 47, 5, 14, 12], semi-circular [48, 49, 7], rectangular [50, 51, 52, 53, 54], families of sine waves [55], and trapezoidal [56, 57, 54] have been considered before. Due to the difference in the shapes of the textures, various physical dimensions (height, spacing, radius of curvature, etc.) have been used to compare the frictional drag response of the textures; height and spacing of the texture elements are universally applicable to any periodic 2D texture, but other geometric features (corner angles, the radii of curvatures, etc.) are shape-specific and not expandable to other shapes, and descriptive names only offer the means for qualitative comparison of the performance among the variety of textures.

Here, a polynomial framework is proposed to quantitatively define the shape of the textures, and allow for an objective comparison among the various families of grooves. While the scope

*Corresponding author.

Email address: sraayai@fas.harvard.edu (Shabnam Raayai-Ardakani)

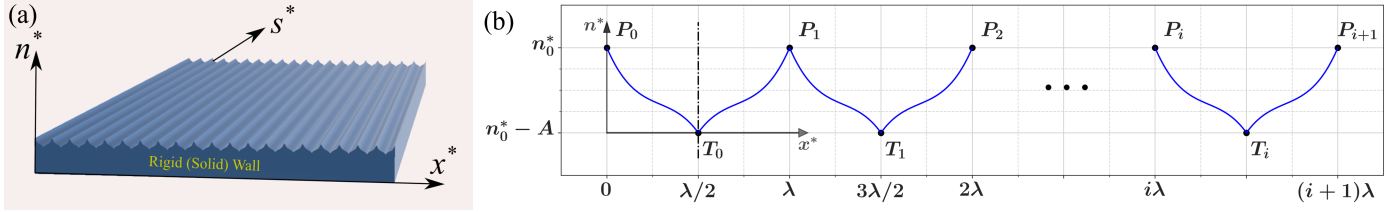


Figure 1: (a) Three dimensional schematic of a periodic, symmetric, 2D texture on a rigid solid wall; (b) Projection of the 2D profile on the (x^*-n^*) plane. The horizontal distance between consecutive peaks (P_i and P_{i+1}) and troughs (T_i and T_{i+1}) is the spacing, λ , and the vertical distance between peaks and troughs is A . The profile is λ -periodic, and symmetric about lines of $x^* = j\lambda/2$, where $j \in \mathbb{N}$. One example of a symmetry line is presented with a dashed-dotted line at $x^* = \lambda/2$.

of this work is focused on textures in hydrodynamic applications to optimize the frictional drag force, the mathematical classification of the textures can be expanded to other scientific applications as well. Here, the performance of the surfaces is evaluated using experimental and numerical analysis of the textures in a Taylor-Couette (TC) flow [58, 9, 10] especially focusing on the frictional torque (equivalent to drag in cylindrical coordinate system) response of the surfaces in cylindrical Couette flow regime (CCF) as the key measure of comparison.

Methods

Experimental procedure

The experiments were conducted using a custom-designed and built Taylor-Couette (TC) cell (Fig. 2) attached to a stress-controlled rheometer (TA Discovery Hybrid Rheometer 2). The radius ratio of the TC cell is kept at $\eta = R_i/R_o = 0.65$ and the height ratio $\Gamma = L/(R_o - R_i) = 5.1$ where R_o and R_i are the radii of the outer cylinder and the inner cylinder respectively, and L is the length of the rotor (Fig. 2). Here, the outer cylinder is kept stationary ($\Omega_o = 0$), the inner cylinder rotates at a rotation rate of Ω_i , and the torque experienced by the rotor, $\mathcal{T}_{\text{total}}$, is measured via the sensors in the rheometer. Further details of the design of a similar TC cell can be found in Ref. [10].

Textured covered rotors were 3D printed via stereo-lithography (Formlabs Form3 3D printer and photopolymer resin). The design of the full rotors comprise of the inner rotor (which is in contact with the working fluid during the experiments) and a sleeve with a tapped hole that allows for the rotors to be installed on the rheometer and be connected to the sensors (Fig. 2). The outermost radius of the textured cylinders (i.e. texture peak) is at R_i and the smallest radius of the textures is located at the trough at $R_i - A$, where A is the height of the textures (Fig. 1(b)).

The effect of the gap at the closed bottom of the rotor is subtracted from the measured torque using the procedure outlined in Refs. [10, 9]; in summary, the distance between the bottom of the rotor and the TC cell (h_b) is calibrated using

$$\mathcal{T}_{\text{bottom}} = \mu \frac{\pi R_i^4}{2h_b} \Omega_i \quad (1)$$

and set to $h_b = 340 \mu\text{m}$, and using Eq. (1) the excess torque from this bottom effect is then subtracted from all measurements (i.e. $\mathcal{T} = \mathcal{T}_{\text{total}} - \mathcal{T}_{\text{bottom}}$).

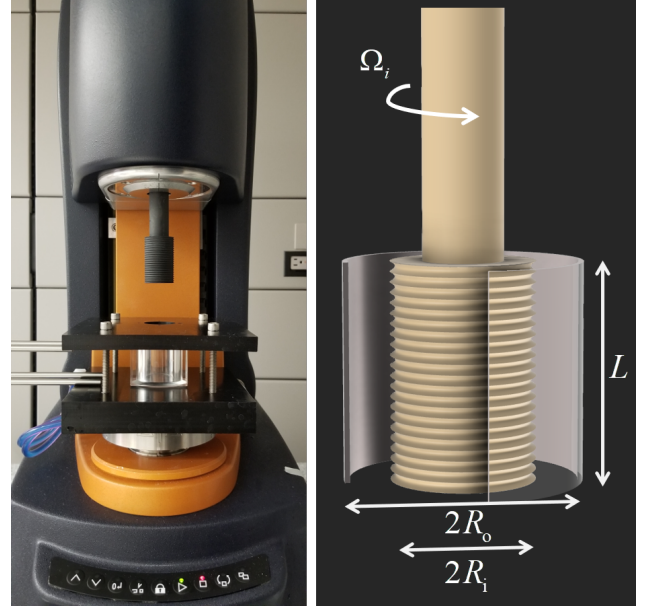


Figure 2: Image of the experimental Taylor-Couette setup, attached to a stress-controlled rheometer on the left, and a schematic of the setup, on the right.

The working fluid is a mixture of 70% Glycerol (Sigma Aldrich BioXtra $\geq 99\%$) and 30% de-ionized water (volumetric ratio) and the viscosity of the working fluid is measured at the beginning and the end of the experimental procedure as a function of temperature. To account for any affect of temperature on the viscosity of the working fluid, throughout the experiment temperature of the fluid and the surrounding environment is measured in 60 second intervals using a two channel thermometer (Digi-sense Tracable Memory-loc Datalogging Thermometer) and the fluid temperature is used to adjust the viscosity of the working fluid during data analysis. The maximum temperature change recorded in either channel of the thermometer, during each experimental procedure is less than $0.5\text{-}0.8^\circ \text{C}$ (viscosity variation within 2% of the average viscosity), and while this variation is accounted for in the analysis, turns out to have a negligible effect on the results. (This can also be shown using the Nahme-Griffith number [9].) The density of the mixture is calculated using the formula given in Ref. [59].

The rotation rates, and torque, as well as fluid properties are used to calculate the Reynolds number and the dimensionless torque (following the definition from references [60, 61]) using

$$\text{Re}_d = \frac{\rho(R_o - R_i)R_i\Omega_i}{\mu} \quad (2)$$

and

$$G = \frac{\mathcal{T}}{4\pi\rho\nu^2L} \quad (3)$$

where ρ , and μ are the fluid density and dynamic viscosity respectively, and $\nu = \mu/\rho$.

For the purpose of comparison, a smooth rotor with inner radius of R_i , and length L is also tested with the same procedure. The measured dimensionless torque for the smooth rotor G_0 (after subtraction of the bottom effect) is on average within 0.6% of the theoretical torque

$$G_{\text{th}} = \frac{\eta}{(1 - \eta^2)(1 - \eta)} \text{Re}_d \quad (4)$$

in CCF regime within $10 \leq \text{Re}_d \leq 40$ and within 2% of the theoretical torque within $40 < \text{Re}_d \leq 60$ (average). The measured G_0 is used throughout the text to normalize the torque of the rest of the samples. These measured torques and Reynolds numbers were used to identify the onset of transition to the Taylor vortex flow, $\text{Re}_{d,\text{tr}} = 64$, following the method described in Refs. [60, 61].

The experimental procedure used here is based on a set of 60-step ‘‘peak hold’’ procedures were at each step a constant rotation rate is imposed on the inner rotor for a span of 15 seconds and torque is read five times during these 15 seconds and an average of these five readings is used for the analysis ($\mathcal{T}_{\text{total}}$). This ‘‘peak hold’’ is repeated for velocities corresponding to CCF regime (i.e. Reynolds numbers less than $\text{Re}_{d,\text{tr}} = 64$). Measurements for the textured surfaces didn’t present any sign of transition happening earlier than $\text{Re}_d = 64$. Each set of experiment is then repeated 6 times and the results are presented here as mean \pm one standard deviation.

Numerical simulations

For comparison, direct numerical simulation of the CCF over textured surfaces are conducted using the finite volume package, OpenFOAM. The simulations are performed for one single unit of texture, in axisymmetric, steady-state conditions, using the SIMPLE algorithm, with periodic boundary conditions at $x^* = 0$, and $x^* = \lambda$. Here the diffusion terms are discretized with a second-order central difference, and the convective terms are discretized with a second-order central difference with correction for the non-orthogonality of the mesh faces due to the textures.

Results

Periodic, symmetric 2D textures

A 2D periodic texture (Fig. 1(a)), consists of symmetric unit elements (between a peak-trough-peak group, P_i , T_i , and P_{i+1} - Fig. 1(b)) where the streamwise and spanwise directions are denoted by s^* and x^* and the normal to the two directions is denoted by n^* (all starred variables are dimensioned). The

unit of texture has a spacing of λ (i.e. $(x_{P_{i+1}}^* - x_{P_i}^*) = (x_{T_{i+1}}^* - x_{T_i}^*) = \lambda$) and height of A (i.e. $(n_{P_i}^* - n_{T_i}^*) = A$), and half of the symmetric profile of the wall in between P_i and T_i is defined by a function $n_w^* = f^*(x^*)$. Due to the symmetry, all directions are non-dimensionalized by half of the wavelength ($s = s^*/(\lambda/2)$, $x = x^*/(\lambda/2)$, $n = n^*/(\lambda/2)$), and the height-to-half-spacing ratio is denoted by $\mathcal{R} = A/(\lambda/2)$ (i.e. $(x_{T_i} - x_{P_i}) = 1$, and $(n_{P_i} - n_{T_i}) = \mathcal{R}$). Here, it is assumed that all peaks and troughs are located at $n = n_0$ and $n = n_0 - \mathcal{R}$ respectively (where n_0 is an arbitrary point of reference and can be shifted to any choice of reference point and coordinate system) and for all the cases considered here, the domain located above the texture profile ($n > n_w$) is filled with fluid and the domain below this boundary ($n < n_w$) is a rigid wall.

With this setting, for textures with the same peak and trough locations, function f is the key to distinguishing between textures of different shapes. For example, in the simplest form, one can set f to be a line connecting P_i and T_i , in the form of

$$n_w = -\mathcal{R}x + n_0 \quad \text{for } 0 \leq x \leq 1 \quad (5)$$

where \mathcal{R} , or the height-to-half-spacing ratio is also the magnitude of the slope of the function f (in $0 < x < 1$). This functional form returns the triangular or V-groove textures that have been considered extensively in literature [8, 4, 47, 5, 14, 12]. In a similar manner, $n_w = n_0$ returns the case of a smooth reference surface.

Concavity and convexity

When considering a curved (or non-linear) profile, f , for each unit element of the texture, after an average slope, \mathcal{R} , (i.e. height-to-half-space ratio), concavity becomes a second geometric feature that is considered. With concavity defined as $d^2n_w/dx^2 > 0$ (and vice versa convexity as $d^2n_w/dx^2 < 0$) the simplest function representing a curved texture has a constant second derivative, resulting in a second order polynomial of the form $n_w = a_2x^2 + a_1x + a_0$ where $2a_2$ is the constant second derivative and a_1 and a_0 are found based on \mathcal{R} , and the choice of n_0 . If the constant second derivative is given as $2\kappa_2$, then f is written as

$$n_w = \kappa_2x^2 + (-\kappa_2 - \mathcal{R})x + n_0 \quad 0 \leq x \leq 1. \quad (6)$$

For textures where the peaks and troughs are the only global (and local) extrema, the profile of the textures, f , needs to be locally monotonic between each peak-trough segment and this results in κ_2 being bounded by the limits $-\mathcal{R} \leq \kappa_2 \leq \mathcal{R}$ (Fig. 3(a)). The definition of the profile as written in Eq. (6) decomposes the effect of the texture geometry into two terms identified by the height-to-half-spacing ratio, \mathcal{R} , and κ_2 , as a curvature parameter. Therefore, if $\kappa_2 = 0$ (i.e. $d^2n_w/dx^2 = 0$), f returns the profile of a triangular texture (Eq. (5)). At a constant \mathcal{R} , varying κ_2 from its lowest ($\kappa_2 = -\mathcal{R}$) to highest ($\kappa_2 = \mathcal{R}$) limits, results in a series of textures spanning from convex ($\kappa_2 < 0$) to concave ($\kappa_2 > 0$) profiles (Fig. 3).

Experimental and numerical evidence show that varying κ_2 directly affects the frictional response of the flow in the laminar regime. 3D printed texture-covered inner rotors with $\mathcal{R} = 0.50$,

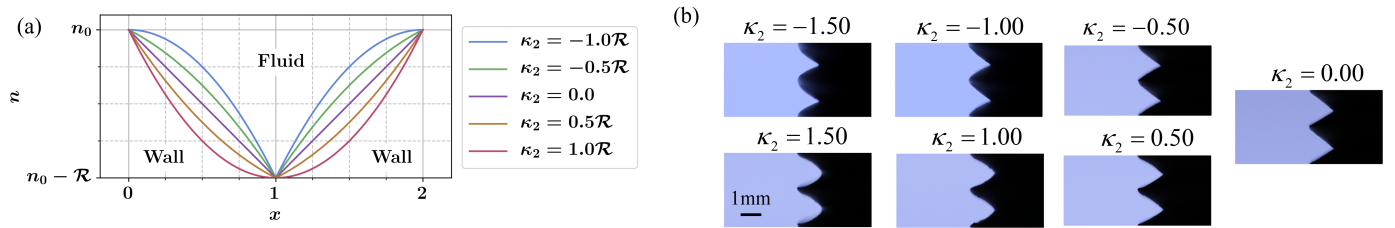


Figure 3: (a) Family of curved textures, defined by second order polynomials with height-to-half-spacing of \mathcal{R} , and $-\mathcal{R} \leq \kappa_2 \leq \mathcal{R}$. (b) Profiles of two unit textures on the surface of 3D printed rotors covered with second order textures with $\mathcal{R} = 1.50$ and $-1.50 \leq \kappa_2 \leq 1.50$.

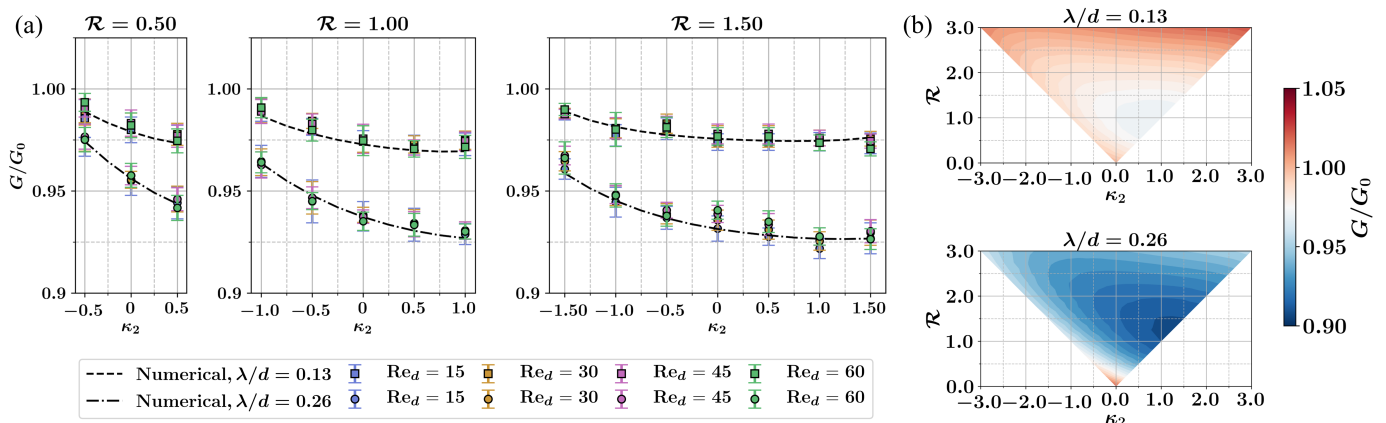


Figure 4: (a) Dimensionless torque experienced by textured rotors with profiles defined by second order polynomials, with $\mathcal{R} = 0.50, 1.00,$ and 1.50 , and $\lambda/d = 0.13$, and 0.26 as a function of κ_2 . Torque is normalized by the torque experienced by the smooth rotor. (b) Contours of dimensionless torque of textured rotors with a profile defined by second order polynomials as a function of \mathcal{R} , and κ_2 , normalized by the torque of a smooth rotor, G_0 , calculated numerically, for grooves with $\lambda/d = 0.13$ (top), and $\lambda/d = 0.26$ (bottom). Sample lines from the contour plots of G/G_0 for select height-to-half-spacings are plotted in Fig. 5 for additional clarity.

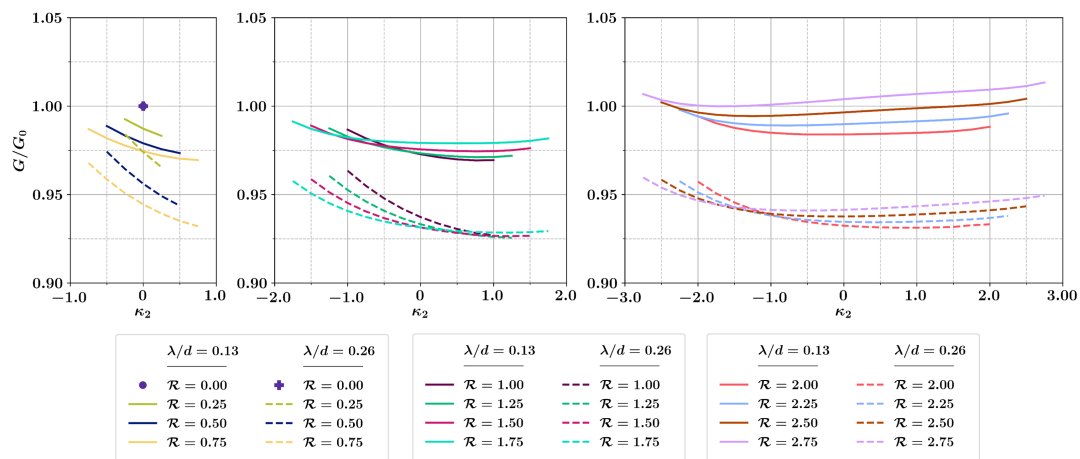


Figure 5: Line plots of torque normalized by the torque of a smooth rotor for select height-to-half-spacing ratios as a function of κ_2 , and $\lambda/d = 0.13$, and 0.26 , corresponding to the contour plots in Fig. 4(b).

1.00, and 1.50 and various values of κ_2 (Fig. 3(b)) are tested in the CCF regime and the frictional torque experienced by the rotors (\mathcal{T}) is measured as a function of the rotation rate, Ω_i , of the inner rotors. In this cylindrical setting, r , θ , and x are the respective normal, streamwise, and spanwise directions. The measurements (Fig. 4(a)) are presented in terms of dimensionless torque, G , normalized by reference G_0 of a smooth rotor, as

a function of \mathcal{R} , κ_2 , and the Reynolds number of the flow, Re_d .

While independent of the Reynolds number (similar to the previous reports for CCF [9, 10]), for all samples (Fig. 4(a)), decreasing κ_2 from zero (i.e. moving from a triangular profile toward a convex profile) results in an increase in the torque compared to that of the V-grooves ($\kappa_2 = 0$). However, for $\mathcal{R} = 0.50$ and 1.00 increasing κ_2 from zero (moving from tri-

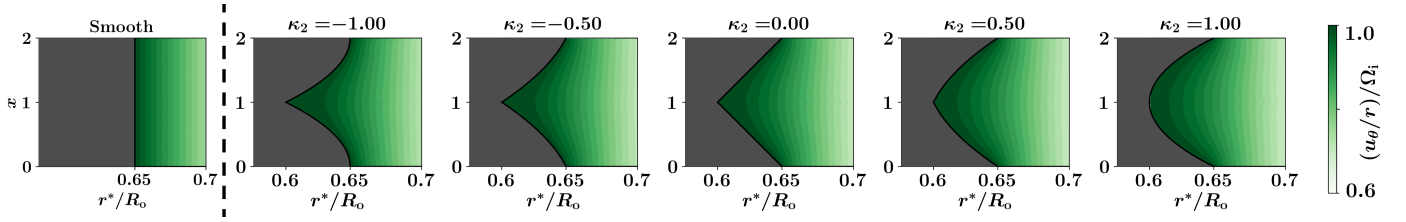


Figure 6: Distribution of the angular velocity (u_θ/r^*) normalized by the angular velocity of the inner rotor (Ω_i) for textures with $\mathcal{R} = 1.00$, and $-1 \leq \kappa_2 \leq 1$. Angular velocity of a smooth case is presented on the left for comparison.

angular to a concave texture) results in a reduction in the measured torque with respect to the triangular texture. This is while for $\mathcal{R} = 1.50$, the same increase in κ_2 does not offer a substantial change. These trends are similar to two aspects of previous reports of tests using curved textures in turbulent flow in wind tunnel; First, between triangular, and semi-circular textures in concave and convex format, concave textures reduce the drag force the most; triangular textures present less reduction compared to the concave ones, and convex ones do not show any difference compared with a smooth wall [8]. Second, increasing the radius of curvature of troughs of grooves results in enhancements in the total drag reduction achieved, while increasing the radius of the curvature at the peaks, results in an increase in the total measured drag force [7]. On the other hand, the current measurements also confirm that (similar to triangular textures [9, 10]) employing a larger wavelength results in a lower level of torque on the rotors and the introduction of κ_2 does not affect this trend.

Changes in torque as a function of κ_2 are dependent on \mathcal{R} of the grooves (as presented in the contours of Fig. 4(b) and corresponding line plots in Fig. 5); while confirming the trends presented in Fig. 4(a), direct numerical simulations of textures with $0 \leq \mathcal{R} \leq 3$ and $\lambda/d = 0.13$ and $\lambda/d = 0.26$ show that for profiles with $\mathcal{R} \leq 1.00$, going from a convex to a concave profile offers a decrease in the measured torque; textured rotors with $1.00 < \mathcal{R} \leq 2.00$ (similar to $\mathcal{R} = 1.50$ in Fig. 4(a)), do not experience a substantial change in the torque for $0 \leq \kappa_2 \leq \mathcal{R}$ while moving toward a convex profile results in an increase in the torque (compared with the V-grooves); and lastly for cases with $\mathcal{R} > 2.00$, the trend slowly reverses where convex profiles experience frictional torques lower than the case of a triangular groove and all concave profiles increase the torque.

Variation in G as a function of κ_2 can be assessed by examining the distribution of angular velocity and consequently the wall shear stress at the textured wall. Contours of the angular velocity of the flow, u_θ/r , (Fig. 6) show that in comparison to a smooth rotor, the iso-lines inside the grooves are curved, mimicking a pattern dictated by the shape of the texture at the boundary (but not exactly the same shape) and as one moves further away from the boundary (Fig. 6 at $r^*/R_o \gtrsim 0.68$) the iso-lines return to being parallel to the x direction. The effect of κ_2 is especially visible at peaks and troughs where for all the textures, the iso-lines are squeezed close to each other at the peaks, but at the troughs the lines are pushed further apart.

In laminar flows, such as the case of the CCF here, viscous diffusion plays the key role in the development of the flow. With

the diffusion occurring in the wall-normal direction and the wall shear stress being proportional to the velocity gradient in the wall-normal direction, employing a coordinate transformation from the generic $(x - n)$ plane to a curvilinear, orthogonal coordinate system of $(\eta - \xi)$ where the iso- ξ and iso- η lines are respectively parallel and perpendicular to the textured boundary, offers additional insight.

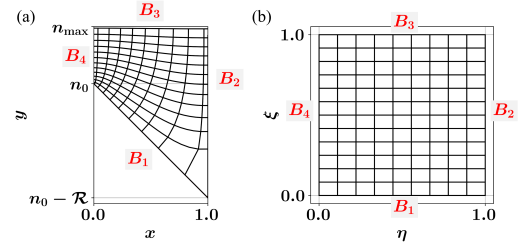


Figure 7: Boundaries of the domain mapped between (a) $(x - n)$ plane and (b) $(\eta - \xi)$ plane resulting in the curvilinear orthogonal coordinate system for an example triangular texture.

To find the curvilinear-orthogonal coordinate system corresponding to each of the texture domains, inverse of an elliptical mapping between the $(x - n)$ coordinate and the new $(\eta - \xi)$ coordinates is employed (Fig. 7). The forward map is defined by Laplace equations of the form

$$\nabla^2 \eta(x, n) = 0 \quad (7)$$

$$\nabla^2 \xi(x, n) = 0 \quad (8)$$

with boundary conditions of

$$\left. \frac{\partial \eta}{\partial h} \right|_{B_1} = 0 \quad \& \quad \left. \xi \right|_{B_1} = 0 \quad (9)$$

$$\left. \frac{\partial \xi}{\partial h} \right|_{B_2} = 0 \quad \& \quad \left. \eta \right|_{B_2} = 1 \quad (10)$$

$$\left. \frac{\partial \eta}{\partial h} \right|_{B_3} = 0 \quad \& \quad \left. \xi \right|_{B_3} = 1 \quad (11)$$

$$\left. \frac{\partial \xi}{\partial h} \right|_{B_4} = 0 \quad \& \quad \left. \eta \right|_{B_4} = 0 \quad (12)$$

where B_1 is the textured boundary and the rest of the boundaries are numbered B_2 - B_4 in the counter clockwise direction (Fig. 7),

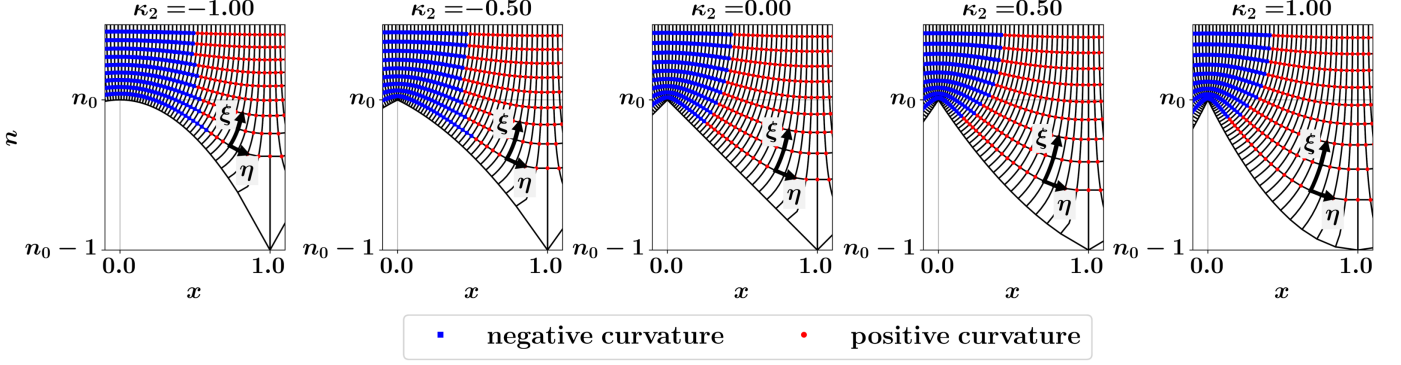


Figure 8: Iso-lines of curvi-linear, orthogonal coordinate system $(\eta - \xi)$, perpendicular to the texture boundary for textures with $\mathcal{R} = 1.00$, and $-1.00 \leq \kappa_2 \leq 1.00$. Locations along the iso- ξ with negative and positive curvature have been marked with blue squares and red circles respectively.

and h is the local normal to the surface at each boundary. Thus the inverse of this mapping [62] is calculated by solving Eq. (13), and Eq. (14)

$$g_{22} \frac{\partial^2 x}{\partial \eta^2} - 2g_{12} \frac{\partial^2 x}{\partial \eta \partial \xi} + g_{11} \frac{\partial^2 x}{\partial \xi^2} = 0 \quad (13)$$

$$g_{22} \frac{\partial^2 n}{\partial \eta^2} - 2g_{12} \frac{\partial^2 n}{\partial \eta \partial \xi} + g_{11} \frac{\partial^2 n}{\partial \xi^2} = 0 \quad (14)$$

where g_{11} , g_{12} , and g_{22} are the metric tensors connecting the two coordinate systems

$$g_{11} = \left(\frac{\partial x}{\partial \eta} \right)^2 + \left(\frac{\partial n}{\partial \eta} \right)^2 \quad (15)$$

$$g_{22} = \left(\frac{\partial x}{\partial \xi} \right)^2 + \left(\frac{\partial n}{\partial \xi} \right)^2 \quad (16)$$

$$g_{12} = \left(\frac{\partial x}{\partial \eta} \right) \left(\frac{\partial x}{\partial \xi} \right) + \left(\frac{\partial n}{\partial \eta} \right) \left(\frac{\partial n}{\partial \xi} \right). \quad (17)$$

The equations are solved iteratively with a python script, using an algorithm similar to the approach presented in [63] subject to the boundary conditions in Eq. (9), Eq. (10), Eq. (11), and Eq. (12).

The trend in the iso- ξ lines match the iso-velocity lines (in Fig. 6) very well and close to the peaks of all the textures ($x \approx 0$ in Figs. 6 and 8), both iso- η and iso- ξ lines are squeezed close to each other, while in the trough area ($x \approx 1$ in Figs. 6 and 8), the distances between the iso-lines are more relaxed.

Such variations in the iso-lines of the $(\eta - \xi)$ coordinate system (Fig. 8) and the angular velocity distribution (Fig. 6) as a function of κ_2 of these textures, directly results in a non-uniform velocity gradient and thus a non-uniform shear stress distribution on the wall as shown in Fig. 9(a) normalized by the shear stress experienced by a smooth rotor, τ_0 . The squeezed iso-lines at the peaks and the spaced out iso-lines in the valleys result in the shear stress at the peaks of all textures to be larger than the shear stress experienced by a smooth rotor τ_0 (line $\tau/\tau_0 = 1.00$ in Fig. 9(a)), while in the troughs τ is lower than τ_0 (similar to previous reports for triangular grooves [5, 9, 64]).

The effect of the curvature of the texture, manifested in the κ_2 parameter, is visible in the local curvature of the iso- ξ lines inside the grooves (the first iso- ξ line is the texture boundary). In all cases, the iso- ξ lines above the peaks have a negative local curvature (blue squares in Fig. 8) and as one moves toward the valleys the curvature slowly increases and turns positive (red circles in Fig. 8). As one moves from convex to concave textures, the extent of the segment of the iso- ξ line with negative curvature slowly recedes and the portion of the iso- ξ line with positive curvature increases.

This variation in the local curvature of the iso- ξ lines causes the distribution of the velocity gradient and the wall shear stress at the riblet-covered wall to span a range of below and above the shear stress on a smooth rotor, τ_0 , and for $\mathcal{R} \geq 0.50$ the points of cross-over between $\tau > \tau_0$ and $\tau < \tau_0$ takes place within $0 < x \leq 0.503$ (Fig. 9(b)). In addition, the reduction in the portion of the iso- ξ lines with negative curvature observed as κ_2 is increased directly results in the $x_{\text{cross-over}}$ to be shifted closer to the peak of the grooves, and thus a larger segment of the textured wall exhibits shear stress values lower than τ_0 . This trend directly results in a decrease in the G values for $\mathcal{R} \leq 1.00$ when κ_2 is increased. In addition, a point-wise comparison of the wall shear stress distribution of the textures with $\kappa_2 \neq 0$ and the wall shear stress of the triangular grooves, τ_1 , (Fig. 10) shows that a large segment of the wall shear of convex textures is placed higher than that of τ_1 and for concave ones, a large portion of each half of the texture has a wall shear stress lower than τ_1 . This ultimately results in convex textures having a larger torque compared to the triangular textures and for concave textures with $\mathcal{R} \leq 1.00$ to have lower torques than the triangular ones. However, for cases with $\mathcal{R} > 1.00$ the level of reduction in the local shear stress compared with τ_1 observed in the $\tau < \tau_1$ portion of the texture for $\kappa_2 > 0$, is nearly similar for all the concave textures, and while the average wall shear stress has a decreasing trend, the total wetted surface area of the texture is increased (Fig. 11), and thus no substantial difference with respect to the triangular textures is seen.

Inflection point

After concavity, the next level of complexity is the possibility of the profile f to possess an inflection point and the sim-

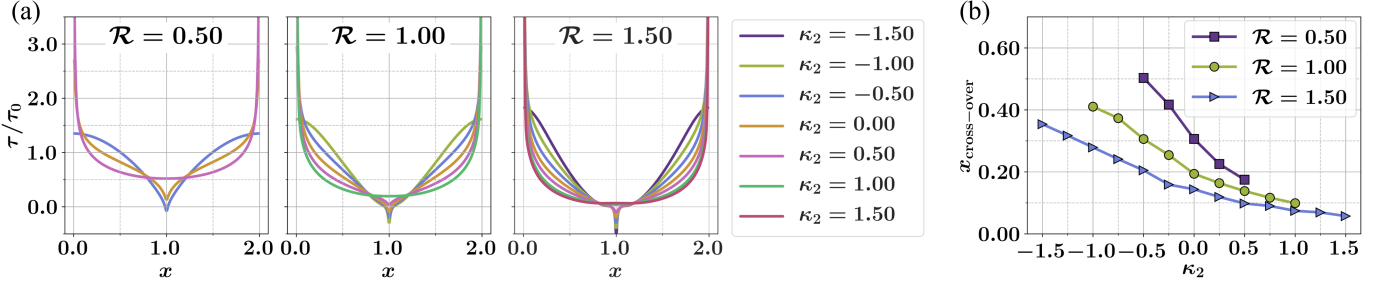


Figure 9: (a) Distribution of wall shear stress as a function of the spanwise location, x , within each texture unit, for textures with second order profiles, $\mathcal{R} = 0.50$, 1.00 , and 1.50 , and $\lambda/d = 0.26$, as a function of $-\mathcal{R} \leq \kappa_2 \leq \mathcal{R}$. (b) Location of point of cross-over of the shear stress from $\tau > \tau_0$ to $\tau < \tau_0$, as a function of κ_2 for textures with $\mathcal{R} = 0.50$, 1.00 , and 1.50 , and $\lambda/d = 0.26$ within $0 \leq x \leq 1$.

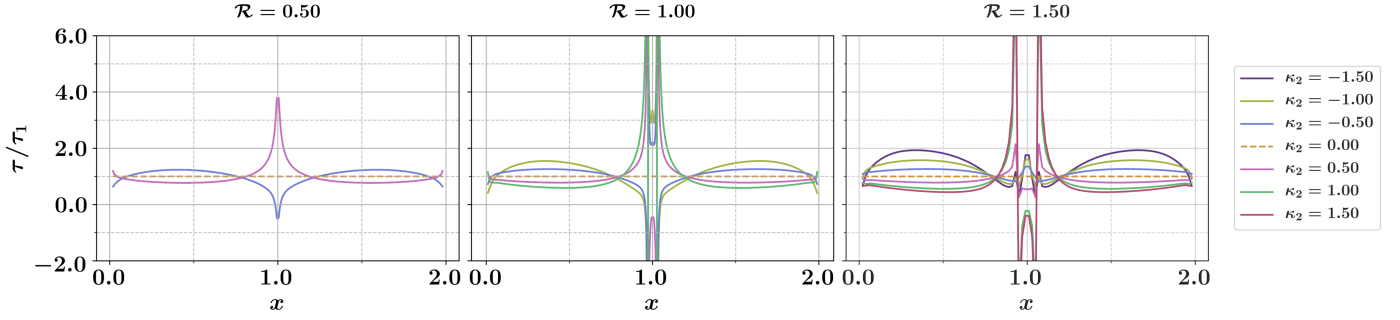


Figure 10: Wall shear stress distribution within one texture element, point-wise normalized by the wall shear stress distribution of a triangular texture, τ_1 , as a function of the spanwise direction, x , for textures defined with second order polynomials with height-to-half-spacing values of $\mathcal{R} = 0.50$, 1.00 , and 1.50 and $\lambda/d = 0.26$.

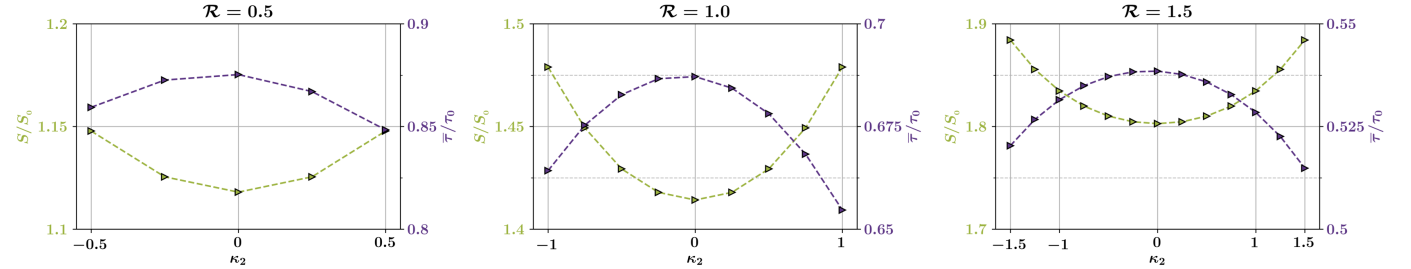


Figure 11: Variations in the average wall shear stress, $\bar{\tau}$, normalized by the shear stress on a smooth rotor, τ_0 (right axis of the plots), experienced by textures defined by second order polynomials as a function of κ_2 with height-to-half-spacing ratios of $\mathcal{R} = 0.50$, 1.00 , and 1.50 and $\lambda/d = 0.26$. The variations in the wetted surface area of the textures, normalized by the surface area of a smooth rotor, S_0 , is also shown as a function of κ_2 (left axis of each plots).

plest function for that is a third order polynomial of the form $a_3x^3 + a_2x^2 + a_1x + a_0$. For a third order polynomial, assuming $d^3n_w/dx^3 = 6\kappa_3$, and an average concavity (the second derivative of the function is no longer constant) defined as

$$\left. \frac{dn_w}{dx} \right|_{x=1^-} - \left. \frac{dn_w}{dx} \right|_{x=0^+} = 2\kappa_2 \quad (18)$$

and height-to-half-spacing ratio of \mathcal{R} , we have:

$$n_w = \kappa_3 x^3 + \left(-\frac{3}{2}\kappa_3 + \kappa_2 \right) x^2 + \left(\frac{\kappa_3}{2} - \kappa_2 - \mathcal{R} \right) x + n_0, \quad (19)$$

where at a constant \mathcal{R} , to keep the textures monotonic in $0 \leq x \leq 1$, the limits of κ_2 and κ_3 are defined by

$$-\left(\mathcal{R} - \frac{\kappa_3}{2} \right) \leq \kappa_2 \leq \left(\mathcal{R} - \frac{\kappa_3}{2} \right) \quad (20)$$

for $-\mathcal{R} \leq \kappa_3 \leq 2\mathcal{R}$ and

$$-\sqrt{-3\kappa_3 \left(\frac{\kappa_3}{4} + \mathcal{R} \right)} \leq \kappa_2 \leq \sqrt{-3\kappa_3 \left(\frac{\kappa_3}{4} + \mathcal{R} \right)} \quad (21)$$

for $-4\mathcal{R} \leq \kappa_3 \leq -\mathcal{R}$ (cross-sectional images of 3D printed textures with f defined by Eq. (19) as a function of κ_2 and κ_3 are presented in Fig. 12(a) and 12(b)). Note that if $\kappa_3 = 0$, then Eq. (19) returns back to Eq. (6), and thus this definition encompasses all the textures defined by the lower order polynomials as well. While all third order polynomials have one inflection point in \mathbb{R} , it is not guaranteed that this point resides within the

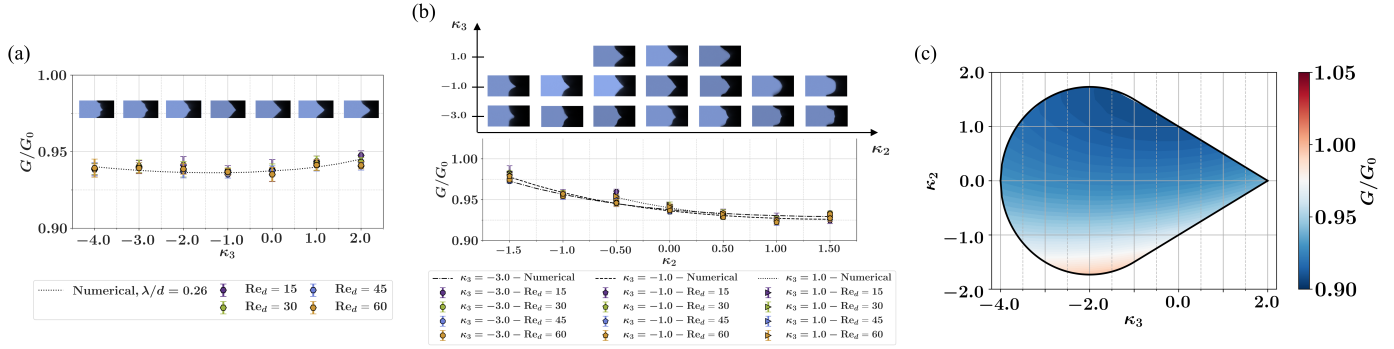


Figure 12: (a) Dimensionless torque experienced by textured rotors defined by third order polynomials, with $\mathcal{R} = 1.00$, $\kappa_2 = 0.00$, and $\lambda/d = 0.26$ as a function of κ_3 . Torque is normalized by the torque experienced by the smooth rotor. Images of samples are presented above the corresponding points. (b) Dimensionless torque experienced by textured rotors with third order profiles, with $\mathcal{R} = 1.00$, $\lambda/d = 0.26$, and $\kappa_3 = -3.00, -1.00$, and 1.00 , as a function of κ_2 . Torque is normalized by the torque experienced by the smooth rotor, G_0 . Images of the samples are presented above the corresponding points. (c) Contours of dimensionless torque of textured rotors with a profile defined by third order polynomials with $\mathcal{R} = 1.00$ as a function of κ_3 , and κ_2 , normalized by the torque of a smooth rotor, G_0 , calculated numerically, for grooves with $\lambda/d = 0.26$.

bounds of $0 \leq x \leq 1$ where profile f is defined and for Eq. (19), only profiles with $|\kappa_2/\kappa_3| < 3/2$ have an inflection point in $0 \leq x \leq 1$.

For textures defined by third order polynomials with $\mathcal{R} = 1$, and $\lambda/d = 0.26$, in the absence of mean concavity/convexity (i.e. $\kappa_2 = 0$), addition of the κ_3 term ($-4 \leq \kappa_3 \leq 2$) does not offer a significant difference in the torque compared to the triangular textures ($\kappa_2 = \kappa_3 = 0$ - Fig. 12(a)) and G in the CCF regime (independent of the Reynolds number) is only marginally affected by κ_3 as found by numerical simulations and experimental results, with the limiting ends ($\kappa_3 = -4$ and $\kappa_3 = 2$) offering slightly larger torque values.

This negligible difference in the response of textures defined by this group of third order polynomials and that of a triangular profile ($\kappa_3 = 0.00$) is further assessed using the wall shear stress distribution at the textured wall normalized by the shear stress of a smooth rotor, τ_0 , and point-wise normalized by the shear stress of a triangular textures, τ_1 , both as a function of the span-wise direction (Figs. 13(a) and 13(b)). In all cases, the wall shear stress distribution oscillates about the wall shear stress of the triangular groove ($\kappa_3 = 0.00$, marked by dashed lines on Figs. 13(a) and 13(b)); for $\kappa_3 < 0$ the shear stress distribution twice crosses over the wall shear stress of the triangular textures where along x within $0 < x < 1$, it is initially lower, then higher, and then lower than the wall shear stress of the triangular grooves. For $\kappa_3 > 0$, the cross-over happens three times where close to the peak, for a small portion, the wall shear stress is lower than the triangular case, and then moves to higher, then lower, and ultimately higher than the wall shear stress for the triangular textures. (Note that the point closest to $x = 1$ that seems like a cross-over in τ/τ_1 in Fig. 13(b) is due to the τ_1 changing sign close to the trough and at this point $\tau/\tau_1 \rightarrow \infty$.) As a result of this oscillation for both positive and negative κ_3 , the changes in the wall shear stress cancel each other out. In addition, while the average shear stress of each of these textures is lower than that of a triangular texture (Fig. 15(a)), the excess wetted surface area of the textures with $\kappa_3 \neq 0$ overcomes the decrease in the average shear stress. All these result

in ultimately a negligible difference in the total frictional torque experienced by this family of textured walls as a function of κ_3 .

While the cross-over of the wall shear stress distributions are also observed in the profiles of textures defined by polynomials of second order (Figs. 9 and 10), the cross-over observed close to $x \approx 1/2$ is due to the presence of the inflection point at $x = 1/2$. The effect of the inflection point is clear in the distribution and the curvature of the iso- ξ lines (Fig. 14) inside these grooves. For $\kappa_3 < 0$, the iso- ξ lines are clustered close to each other at the peaks, and as one moves along x , they slowly become distant, until reaching close to the inflection point where the lines cluster together and then again grow apart close to the troughs. As a result of this, unlike the case of the profiles defined by second order polynomials, close to the texture wall for cases with $\kappa_3 < 0.00$, a portion of the iso- ξ lines past the inflection point at $x = 1/2$ has a negative curvature, which also corresponds to the region with $\tau/\tau_1 > 1.00$.

Similarly, for the rest of the third order textures with $\mathcal{R} = 1$, $\lambda/d = 0.26$, $\kappa_3 \neq 0.00$ (Figs. 12(b), 13(c), and 15(b)), the trend in the measured torque in CCF regime is nearly insensitive to κ_3 and is primarily dependent on κ_2 . Similar to the case of $\kappa_2 = 0.00$, the oscillation of the wall shear stress distribution of the cases with $\kappa_3 \neq 0.00$ around the wall shear stress distribution of the texture with the same κ_2 and $\kappa_3 = 0.00$ results in nearly similar levels of torque among textures with constant κ_2 and different κ_3 terms. Also, gathering the results of the numerical simulations of all third order textures into a contour plot of normalized torque as a function of κ_2 and κ_3 (Fig. 12(c)) shows that the changes are dominantly happening along the κ_2 axis and the changes along the κ_3 axis are minor.

A generalized mathematical framework for construction of symmetric and periodic 2D textures

The complexity of a texture profile is then extended by considering a polynomial of J -th order. To generalize the definition, suppose we want to generate the profile of a texture, f , in the form of a function characterizing the local height of

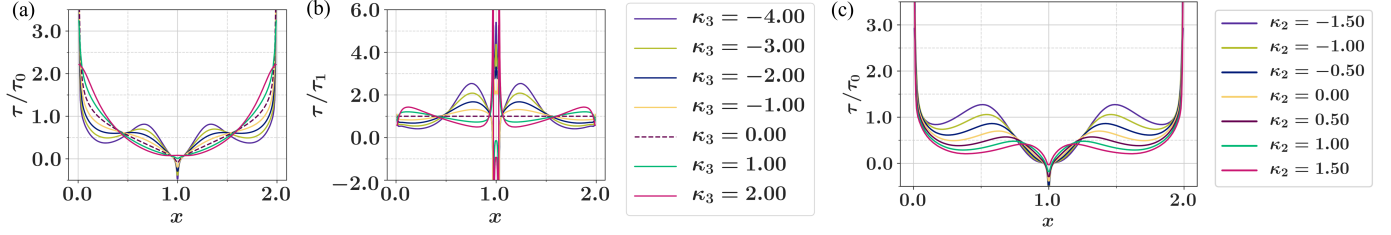


Figure 13: Distribution of wall shear stress for textures with $\mathcal{R} = 1.00$, $\lambda/2 = 0.26$, and $\kappa_2 = 0.00$, normalized by (a) the shear stress of smooth rotor, τ_0 , and (b) point-wise normalized by the shear stress of a triangular groove ($\kappa_2 = \kappa_3 = 0$), τ_1 , as a function of κ_3 and spanwise location, x . (Wall shear stress results for the triangular textures have been additionally marked with dashed lines.) (c) Distribution of wall shear stress for textures defined by third order polynomials with $\mathcal{R} = 1.00$, $\lambda/2 = 0.26$, and $\kappa_3 = -3.00$ as a function of κ_2 and spanwise location, x .

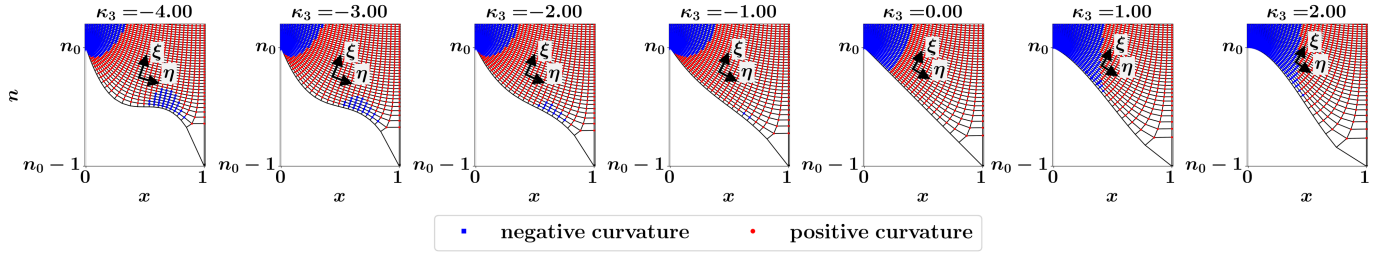


Figure 14: Iso-lines of curvilinear, orthogonal coordinate system ($\eta - \xi$) inside grooves, defined by third order equation Eq. (19), with $\mathcal{R} = 1$, $\lambda/d = 0.26$, and $\kappa_2 = 0$ as a function of κ_3 . Red circles and blue squares denotes segments of the iso- ξ lines with positive and negative curvature respectively.

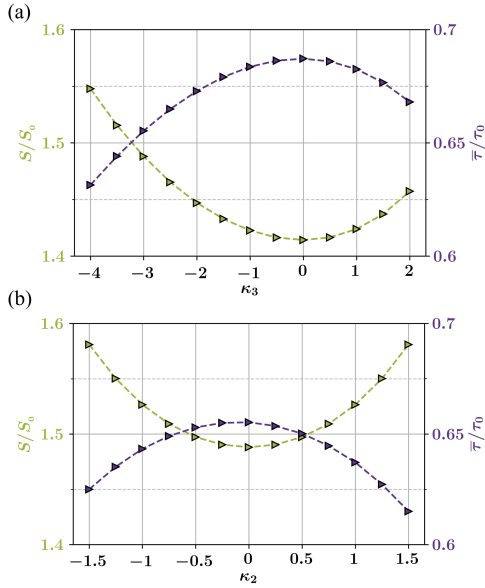


Figure 15: Variations in the average wall shear stress, $\bar{\tau}$, normalized by the shear stress on a smooth rotor, τ_0 (right axis of the plots), experienced by textures defined by third order polynomials with $\mathcal{R} = 1.00$, $\lambda/d = 0.26$, and (a) $\kappa_2 = 0.00$ as a function of κ_3 , and (b) $\kappa_3 = -3.00$ as a function of κ_2 . The variations in the wetted surface area of the textures, normalized by the surface area of a smooth rotor, S/S_0 , is also shown for both cases (left axis of each plots).

the texture in between each peak-trough ($P_i - T_i$) segment within $0 \leq x \leq 1$ (Fig. 1(b)). Let the profile of the textures to be of the form of a polynomial

$$n_w = \sum_{j=0}^J a_j x^j \quad 0 \leq x \leq 1 \quad (22)$$

where J or the degree of polynomial is a measure of the geometric complexity of the texture. Coefficients a_j can take any value, however, here, the domain of each of the coefficients is limited to ensure the all profiles pass through the chosen P_i and T_i ; the profiles are continuous everywhere; the derivatives of the profiles are continuous everywhere except at the peaks and troughs of the textures; chosen peaks and troughs of the function are the only global extrema of the function, and no local minima and/or maxima is allowed within $0 < x < 1$.

While any family of functions can be a valid choice for mathematically representing the shape of the profiles, polynomials not only have the ability to capture some of the most popular texture profiles (as shown earlier) but also allow for gradually increasing the complexity of the textures by changing the degree J ; Using Eq. (22) with $J = 0$ (the zeroth order), $n_w = n_0$ returns the smooth reference surface (i.e. case of $\mathcal{R} = 0$), and $J = 1$ creates the V-groove (or triangular) profile with $a_0 = n_0$ and $a_1 = -\mathcal{R}$ (Eq. (5)).

For the first order, height and spacing of the texture are sufficient to uniquely define the profiles and the coefficients a_0 and a_1 . However, from the second order forward, there is no geometric guide dictating the boundary conditions to define the value of the coefficients and variations in values of a_j ($j \geq 2$) results in more complicated texture profiles, while keeping the wavelength and height-to-half-spacing constant. At each j level, the effect of $a_j x^j$ monomial can be decomposed into two portions, one part is entirely responsible for the ef-

fect of j th order and the other portion ensures that the profile passes through the given peaks and troughs. Let's assume that the portion of the a_j coefficient responsible for the effect of the level of complexity, j , is represented by the parameter κ_j (all κ_j independent of each other), and is defined as the difference of the $(j-1)$ th derivative of the profile at the (limits of) peak and trough normalized by $j!$. Thus for $2 \leq j \leq J$

$$\frac{d^{(j-1)}n_w}{dx^{(j-1)}} \Big|_{x=1^-} - \frac{d^{(j-1)}n_w}{dx^{(j-1)}} \Big|_{x=0^+} = j! \kappa_j \quad (23)$$

and for $j = 1$

$$n_w \Big|_{x=1} - n_w \Big|_{x=0} = 1! \kappa_1. \quad (24)$$

and $\kappa_0 = n_0$ is entirely dependent on the choice of the reference surface. As a result, coefficients a_j , can be decomposed into weighted sums of the κ_l where $l \geq j$, separating the effect of each order,

$$a_j = \sum_{l=j}^J \kappa_l m_{lj} \quad (25)$$

and ultimately collecting all m_{lj} coefficients in matrix \mathcal{M} we can write n_w in the form

$$n_w(x) = \begin{bmatrix} \kappa_0 & \kappa_1 & \cdots & \kappa_J \end{bmatrix} \mathcal{M} \begin{bmatrix} x^0 \\ x^1 \\ \vdots \\ x^J \end{bmatrix}. \quad (26)$$

Based on this definition, \mathcal{M} is a lower triangular matrix where $m_{00} = m_{11} = \cdots = m_{JJ} = 1$ and the rest of the coefficients of each column can be calculated using Eq. (23) and Eq. (24). From the boundary conditions, for all textures we have $\kappa_1 = -\mathcal{R}$ and $\kappa_0 = \mathcal{R}$, and the rest of κ_j can take any value within the physical ranges defined by the conditions described by the user.

The effect of this decomposition can be demonstrated using the two cases studied earlier; a second order profile of the form of Eq. (6), is written as the sum of $\kappa_2(x^2 - x)$, and $-\mathcal{R}x + n_0$. Rewritten this way, the second order profile is decomposed into the profile of a first order texture (Eq. (5)) and a term of second order entirely dependent on κ_2 ; the first monomial, $\kappa_2 x^2$ adds curvature to the profile and the second monomial $-\kappa_2 x$ ensures that the addition of the $\kappa_2 x^2$ does not violate the requirement of the profile passing through the designated peaks and troughs (Fig. 16(a)). Similarly, the third order profile of Eq. (19) can be written as the sum of $\kappa_3(x^3 - 3/2x^2 + 1/2x)$ (a third order part identified by the κ_3) and Eq. (6) (Fig. 16(b)). Thus, this decomposition, separates the effect of each level of complexity while also including the effect of lower order terms within its definition. This results in textures defined by lower order polynomials to be subsets of those defined by higher orders and allowing for easier comparison across shapes (i.e. setting $\kappa_j = 0$ returns the family of textures defined by order $J-1$). Thus, the decomposition of the coefficients of the polynomials using this definition of the κ_j allows for successive expansion of the texture profiles one order at a time toward more complicated

shapes, while keeping the lower order ones among the possible variations.

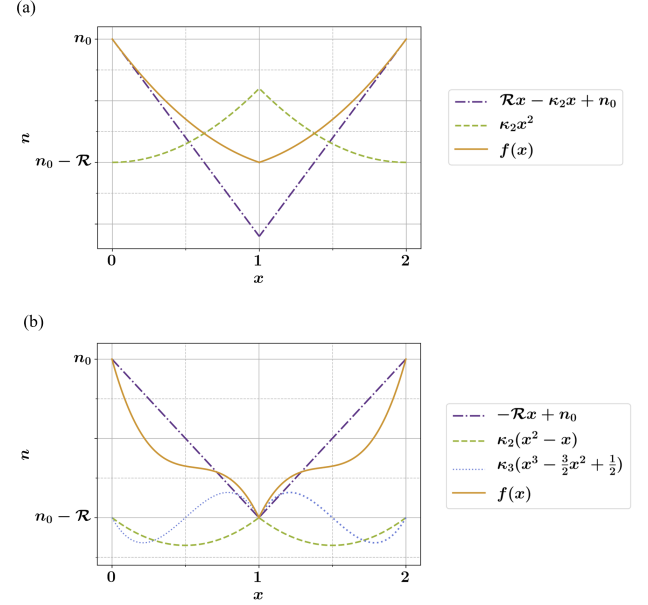


Figure 16: (a) Profile of an example texture, $f(x)$, defined by a second order polynomial decomposed into terms identified by x^0 and x , and x^2 . Note that with $\kappa_2 x^2$ term alone, the profile cannot maintain the location of the peak and trough of the texture, and the $-\kappa_2 x$ monomial is required to satisfy this boundary condition. (b) Profile of an example texture, $f(x)$, defined by a third order polynomial decomposed into terms identified by $\kappa_0 = n_0$ and $\kappa_1 = -\mathcal{R}$, κ_2 , and κ_3 .

Polynomials of order higher than 3, offer a wide range of possibilities to design texture profiles, however, the increase in the complexity does not offer a substantial difference in the hydrodynamic response of these textures in the CCF when compared with the second order textures. Results of experiments and simulations with textures defined by fourth order polynomials of the form

$$n_w = \kappa_4(x^4 - 2x^3 + x^2) + \kappa_3 \left(x^3 - \frac{3}{2}x^2 + \frac{1}{2}x \right) + \kappa_2(x^2 - x) - \mathcal{R}x + n_0 \quad (27)$$

presented in Fig. 17, show that variations in the torque measured with such textures are mainly dictated by κ_2 , and as κ_2 value is decreased, the effect of κ_4 becomes important only in offering a wider variation in the torque, but the variation in the values of torque recorded using textures with fourth order polynomials are within the same range as the variations seen with the second order profiles. In textures with a positive average concavity ($\kappa_2 > 0$) and a constant κ_3 , increase in κ_4 only offers a slight increase in the torque, and analysis of the iso- ξ lines of this sub-family of textures confirms the expansion of a region with negative curvature around $x = 1/2$ which results in the slight increase in the torque (Fig. 18(a)). In the absence of average concavity ($\kappa_2 = 0$), the response of the textures are entirely dependent on the κ_4 parameter and independent of κ_3 , and as κ_4 is increased, the portion of the region close to the wall where the iso- ξ lines have a negative curvature increases. As a

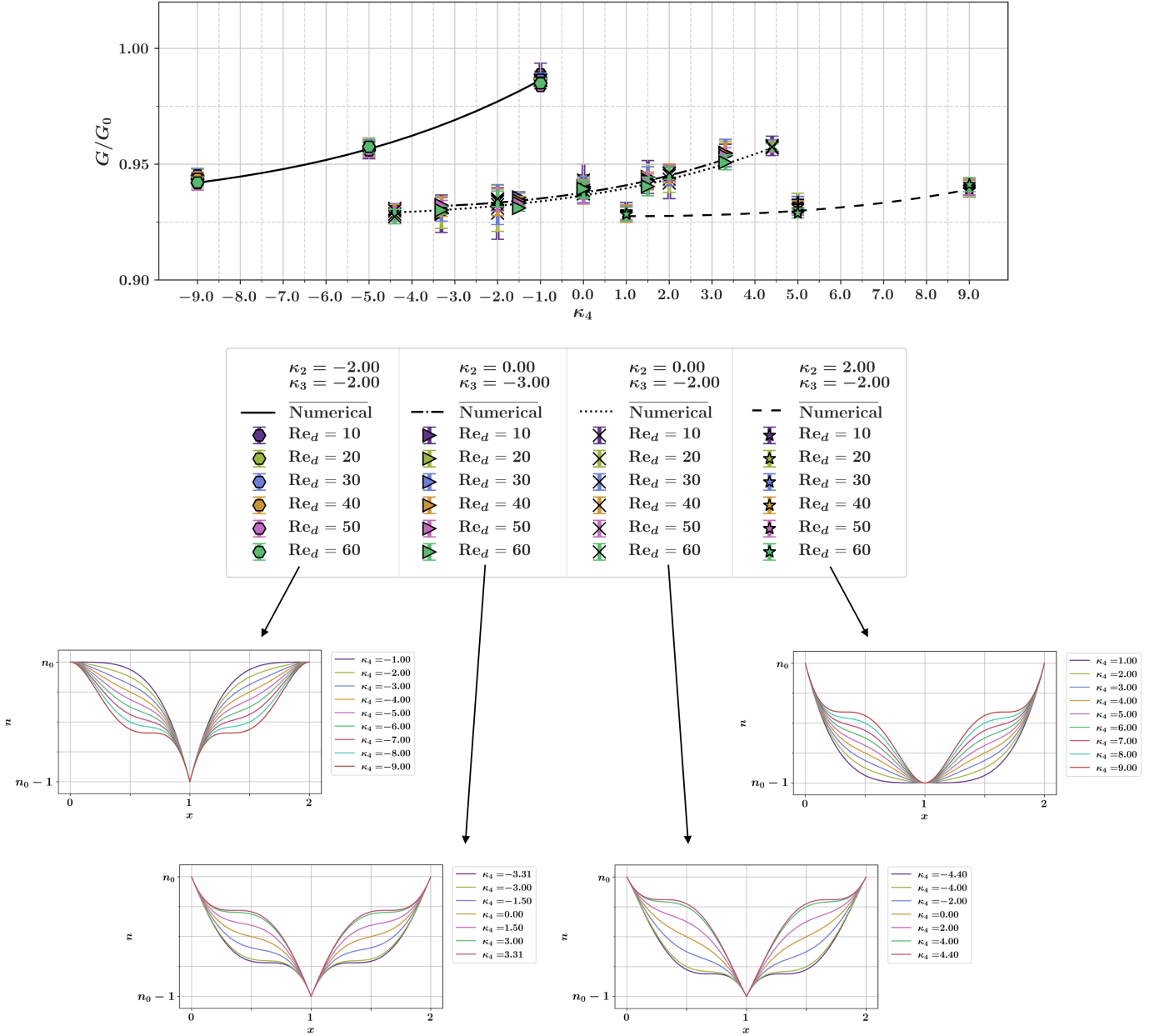


Figure 17: Torque experienced by textured rotors with profiles defined by fourth order polynomials (Eq. (27)) as a function of κ_4 , normalized by the torque of a smooth rotor, G_0 , with $\mathcal{R} = 1.00$, $\lambda/d = 0.26$, and various values of κ_2 and κ_3 . Variations in the shape of the profiles as a function of all the κ parameters of each group are also shown below the plot.

result, within this sub-family of textures, increase in κ_4 results in an increase in the torque (Figs. 17 and 18(b)). As one moves toward $\kappa_2 < 0$ cases, the effect of κ_4 becomes more pronounced allowing for a wider range of torque responses compared to the cases with $\kappa_2 \geq 0$ (Figs. 17 and 18(a)). Overall, in all cases, at constant κ_2 and κ_3 , textures with the lowest κ_4 offer the lowest torque of the sub-family, and increasing κ_4 results in an increase in the portion of iso- ξ close to the wall with negative curvature which directly results in an increase in the total frictional torque within each sub-family considered (Fig. 18).

Families of extreme concave/convex textures

The definition of textures based on polynomials of higher orders allows us to consider families of textures that constitute the two most extreme cases of each order J : the case of textures that are either extremely concave defined by $n_w = \mathcal{R}(1-x)^J + (n_0 - \mathcal{R})$ or extremely convex given by $n_w = -\mathcal{R}x^J + n_0$. (Figs. 19(a) and 19(b) - κ_j coefficients of these textures up to $J = 10$, for $\mathcal{R} = 1$, are listed in Tbls. 1 and 2.) In the extreme concave case as J is increased toward infinity the shape of the texture resembles an idealized form of rectangular (razor blade) textures [53, 57] and for the extreme convex ones as J is increased toward infinity, the profile asymptotically reaches

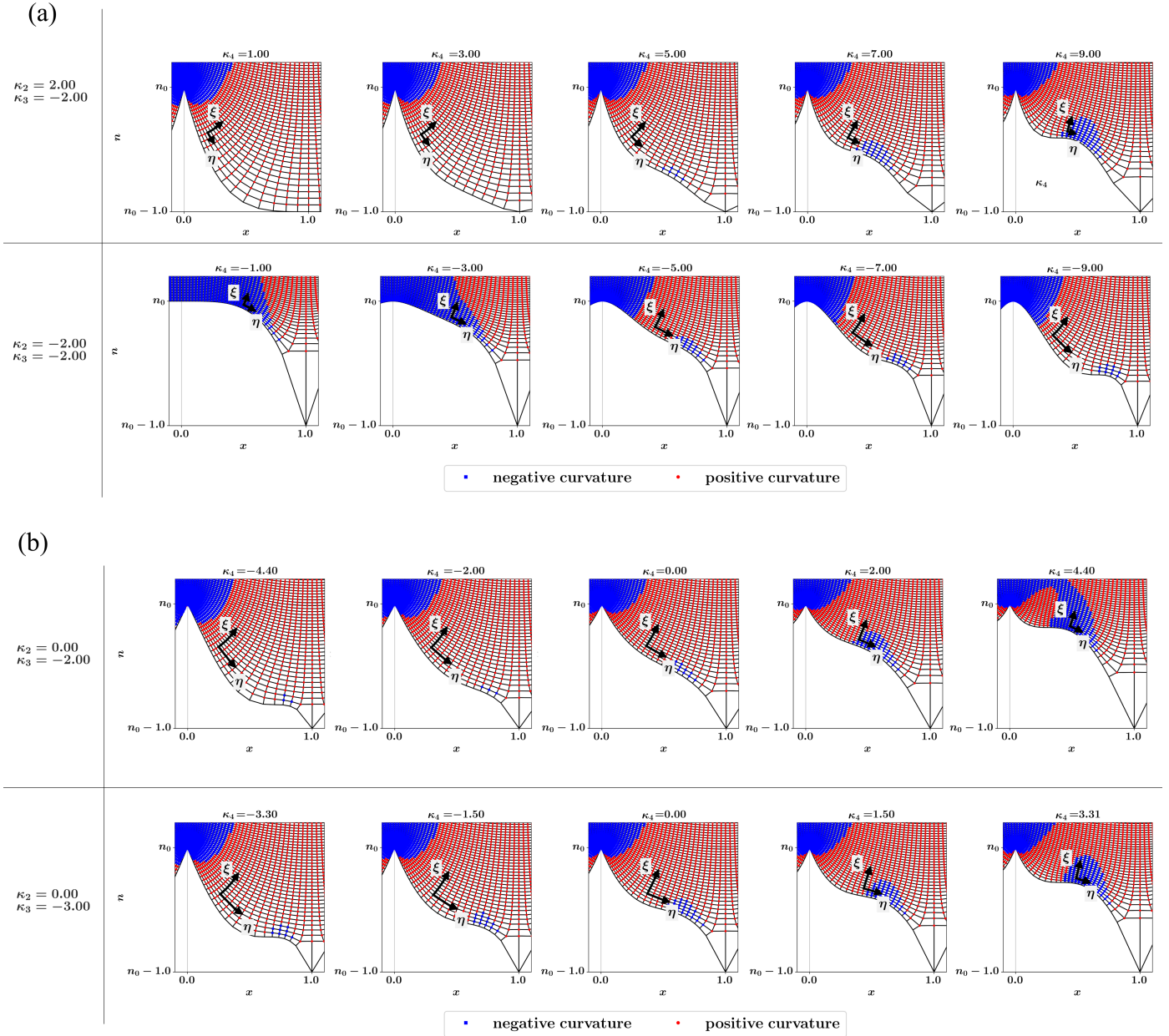


Figure 18: Curvilinear orthogonal coordinates ($\eta - \xi$) for textures defined by fourth order polynomials with $\mathcal{R} = 1.00$ (a) $\kappa_2 = \pm 2.00$, and $\kappa_3 = -2.00$, and (b) $\kappa_2 = 0.00$, $\kappa_3 = -2.00$ and -3.00 as a function of κ_4 values within their allowed limits.

back to the case of a smooth surface. In the concave group, as the order J of the polynomial is increased, the portion of the texture in the vicinity of the trough is smoothed more and more (Fig. 19(a)), and in the convex group, increase in the order of the polynomial results in a wider smooth area at the peak of the textures (Fig. 19(b)). While the increase in the polynomial order of these textures requires additional κ_j terms to define the profile, the increase in the concavity/convexity of these profiles is directly manifest in the increase in the magnitude of the κ_2 term of each profile (Tbls. 1 and 2).

In the case of extreme concave textures ($J \geq 2$), with $\mathcal{R} = 1.00$, and $\lambda/d = 0.26$, textures of order 2 and 3 have a nearly similar torque response (Fig. 19(c)) which is less than the case

of the triangular textures and then beyond that as the order J is increased, the total frictional torque is also increased, and after $J = 7$ it passes to higher than the torque experienced by a triangular texture. On the extreme convex side, for $J \geq 2$ as J is increased (Fig. 19(c)), the torque is also increased and is always higher than torque of a triangular texture and by $J = 7$ it crosses the torque of a smooth surface.

For the family of extreme concave textures ($J \geq 2$), at the trough, the slope of the profiles come to zero and as J is increased a larger segment of the profile in the vicinity of $x = 1$ has a near-zero slope. Reverse of this trend applies to the peaks of extreme convex profiles where near the peaks the segment of the profile with near-zero slope is increased as J is

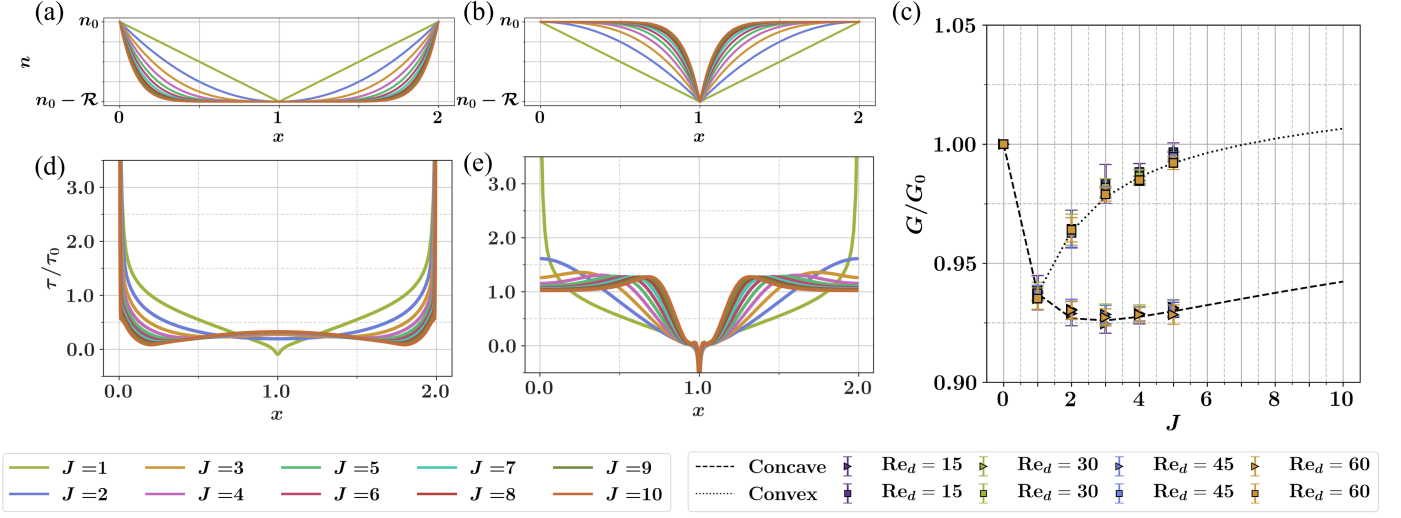


Figure 19: Schematic of families of (a) extreme concave and (b) extreme convex textures of orders 2-10 with arbitrary height-to-half-spacing of \mathcal{R} . Triangular groove ($J = 1$) is shown for reference. (c) Torque experienced by extreme concave (triangular symbol) and extreme convex (rectangular symbol) textures of $\mathcal{R} = 1$, and $\lambda/d = 0.26$, normalized by the torque of a smooth surface. Torque values of a smooth surface and triangular texture ($J = 0$ and $J = 1$) are shown as reference. Results of the direct numerical simulation of concave and convex textures up to $J = 10$ are shown with dashed and dotted lines respectively. Distribution of the wall shear stress normalized by the wall shear stress of a smooth surface as a function of the spanwise direction for (d) extreme concave and (e) extreme convex textures with $\mathcal{R} = 1.00$, and $\lambda/d = 0.26$. The results for $J = 1$ is presented for reference.

Table 1: κ_j values for extreme concave textures for polynomial orders 0-10 for $\mathcal{R} = 1$

Polynomial Order	κ_0	$\kappa_1 = -\mathcal{R}$	κ_2	κ_3	$\kappa_4,$	$\kappa_5,$	$\kappa_6,$	κ_7	$\kappa_8,$	$\kappa_9,$	κ_{10}
$J = 0$	$n_0 - 1$										
$J = 1$	$n_0 - 1$	-1									
$J = 2$	$n_0 - 1$	-1	1								
$J = 3$	$n_0 - 1$	-1	$3/2$	-1							
$J = 4$	$n_0 - 1$	-1	2	-2	1						
$J = 5$	$n_0 - 1$	-1	$5/2$	$-10/3$	$5/2$	-1					
$J = 6$	$n_0 - 1$	-1	3	-5	5	-3	1				
$J = 7$	$n_0 - 1$	-1	$7/2$	-7	$35/4$	-7	$7/2$	-1			
$J = 8$	$n_0 - 1$	-1	4	$-28/3$	14	-14	$28/3$	-4	1		
$J = 9$	$n_0 - 1$	-1	$9/2$	-12	21	$-126/5$	21	-21	4.5	-1	
$J = 10$	$n_0 - 1$	-1	5	-15	30	-42	42	-30	15	-5	1

Table 2: κ_j values for extreme convex textures for polynomial orders 0-10 for $\mathcal{R} = 1$

Polynomial Order	κ_0	$\kappa_1 = -\mathcal{R}$	κ_2	κ_3	$\kappa_4,$	$\kappa_5,$	$\kappa_6,$	κ_7	$\kappa_8,$	$\kappa_9,$	κ_{10}
$J = 0$	$n_0 - 1$										
$J = 1$	$n_0 - 1$	-1									
$J = 2$	$n_0 - 1$	-1	1								
$J = 3$	$n_0 - 1$	-1	$-3/2$	-1							
$J = 4$	$n_0 - 1$	-1	-2	-2	-1						
$J = 5$	$n_0 - 1$	-1	$-5/2$	$-10/3$	$-5/2$	-1					
$J = 6$	$n_0 - 1$	-1	-3	-5	-5	-3	-1				
$J = 7$	$n_0 - 1$	-1	$-7/2$	-7	$-35/4$	-7	$-7/2$	-1			
$J = 8$	$n_0 - 1$	-1	-4	$-28/3$	-14	-14	$-28/3$	-4	-1		
$J = 9$	$n_0 - 1$	-1	$-9/2$	-12	-21	$-126/5$	-21	-21	-4.5	-1	
$J = 10$	$n_0 - 1$	-1	-5	-15	-30	-42	-42	-30	-15	-5	-1

increased. This directly affects the wall shear stress distribution (Fig. 19(d)) where in the extreme concave cases for $J \geq 2$, the local shear stress at the trough of the grooves consistently increases as J is increased and only for $J = 2$, the local shear

stress at the trough is minimum within $0 \leq x \leq 2$ and the minimum local wall shear stress for the rest of the profiles is pushed away from the trough and closer to the peaks. Thus, as order J is increased the average shear stress within the texture profile $\bar{\tau}_j$

takes a decreasing trend (Fig. 20). However, as J is increased, the increase in the wetted surface area results in the the total frictional torque to be the lowest for orders 2 and 3, and then to increases as J is increased. On the extreme convex side, as the order is increased the local wall shear stress at the peak is slowly reduced and asymptotically reaches the value of the wall shear stress of a smooth surface (Fig. 19(e)). However, due to the excess wetted surface area compared to the smooth surface, for $J > 7$ the total frictional torque is slightly larger than that of a smooth surface. With average shear stress $\bar{\tau}_j$ of the convex textures being always larger than that of the concave textures (Fig. 20), even with the decreasing trend (as J is increased), with the increase in the wetted surface area, torque experienced by convex textures takes a monotonically increasing trend as the order is increased ($J > 1$).

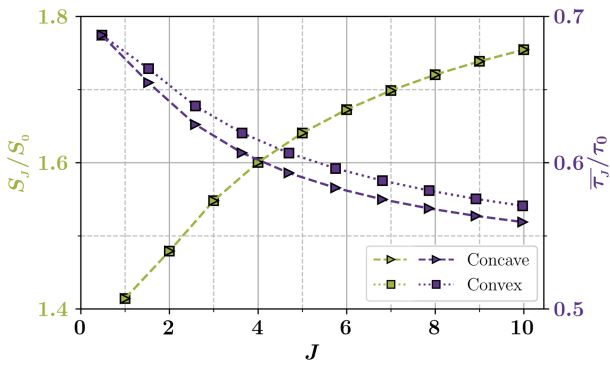


Figure 20: Total wetted surface area, S_j (left axis), and the average shear stress, $\bar{\tau}_j$ (right axis) of extreme concave (triangular symbols) and convex (square symbols) textures as a function of their order J for $J \geq 1$. Wetted surface area is normalized by the wetted surface area of a smooth reference rotor (S_0), and the average shear stress is normalized by the shear stress on a smooth rotor, τ_0 . It is clear that for $J = 0$, $S_j/S_0 = 1$ and $\bar{\tau}_j/\tau_0 = 1$ (not shown).

Ultimately, the comparison of the two extreme concave and convex textures with each other and with the smooth wall and the triangular texture shows that having a near smooth peak is more detrimental to the frictional torque experienced by a texture than having a near smooth trough, and while not the most ideal case, the extreme-concave textures can maintain a torque lower or equal to the level of the triangular textures for $J < 8$ while extreme convex textures can barely maintain the reduction and are not well suited for the purpose of drag reduction in the CCF regime. This can also be a reason for natural textures on shark denticles [2, 65], and peristome of the pitcher plants [25, 26, 27, 28] having a concave form resembling profiles of $J = 2$ or $J = 3$, as opposed to triangular or convex shapes.

Discussion & conclusion

The decomposition of a texture profile into the effects of the κ_j parameters, allows for a more comprehensive understanding of the effect of the geometry of the boundary on the physical response of the surface. Here, with a focus on the hydrodynamic response of the surface in laminar flows, it is clear that after the height-to-half-spacing, the κ_2 parameter, defining the

average level of concavity of a texture plays the most important role in controlling the total frictional response of the surfaces. Textures defined by second order polynomials expand the range of frictional responses compared to the conventional V-grooves, but moving to third and fourth order polynomials does not offer a visible improvement compared to those defined by second order polynomials.

The proposed decomposition can be employed in reverse for any known texture of given profile $n_w = g(x)$ by fitting a polynomial of degree J using a spline interpolation. If the coefficients of the x^j in the spline are b_j , then the values of κ_j terms for this profile can be found by solving the inverse of the linear system of equations in Eq. (25), in the form $\kappa = \mathcal{M}^{-T} \mathbf{b}$ where κ and \mathbf{b} are the vectors consisting of κ_j terms and b_j terms respectively.

It should be emphasized that the shape of polynomials at each degree enables us to create textures with profiles of various levels of complexity and assign quantitative labels to them. As a result of this framework, we are able to move away from qualitative description of texture profiles and track the effect of the geometry not only in terms of the key dimensions of the texture, but also in terms of the dimensionless κ vector that defines all the fine details of the shape of the profiles.

While this work focuses on the hydrodynamic response of surfaces, this framework can easily be expanded to other physical problems where textured surfaces play a role and the effect of each of κ_j parameters can be assessed based on the objectives of the problem of interest.

Declaration of Competing Interest

Author declares no conflict of interest.

Acknowledgements

This work was supported by the Rowland Fellows program at Harvard University.

References

- [1] D. BECHERT, W. REIF, On the Drag Reduction of the Shark Skin, in: 23rd Aerospace Sciences Meeting, Aerospace Sciences Meetings, American Institute of Aeronautics and Astronautics, 1985. doi:10.2514/6.1985-546.
- [2] L. Wen, J. C. Weaver, G. V. Lauder, Biomimetic shark skin: design, fabrication and hydrodynamic function, *Journal of Experimental Biology* 217 (10) (2014) 1656–1666. doi:10.1242/jeb.097097.
- [3] A. Dinkelacker, P. Nitschke-Kowsky, W.-E. Reif, On the possibility of drag reduction with the help of longitudinal ridges in the walls, in: *Turbulence Management and Relaminarisation*, Springer, 1988, pp. 109–120.
- [4] D. Goldstein, R. Handler, L. Sirovich, Direct numerical simulation of turbulent flow over a modeled riblet covered surface, *Journal of Fluid Mechanics* 302 (1995) 333–376.
- [5] H. Choi, P. Moin, J. Kim, Direct numerical simulation of turbulent flow over riblets, *Journal of fluid mechanics* 255 (1993) 503–539.
- [6] M. J. Walsh, Drag characteristics of v-groove and transverse curvature riblets, *AIAA Prog. Astronaut. Aeronaut.* (1980).
- [7] M. J. Walsh, Riblets as a viscous drag reduction technique, *AIAA journal* 21 (4) (1983) 485–486.

- [8] M. Walsh, A. Lindemann, Optimization and application of riblets for turbulent drag reduction, American Institute of Aeronautics and Astronautics, 1984.
- [9] S. Raayai-Ardakani, G. H. McKinley, Geometry mediated friction reduction in taylor-couette flow, *Physical Review Fluids* 5 (12) (2020) 124102.
- [10] S. Raayai Ardakani, Geometry mediated drag reduction using riblets and wrinkled surface textures, Ph.D. thesis, Massachusetts Institute of Technology (2018).
- [11] E. Bacher, C. R. Smith, Turbulent boundary-layer modification by surface riblets, *AIAA journal* 24 (8) (1986) 1382–1385.
- [12] L. Djenidi, L. Squire, A. Savill, High resolution conformal mesh computations for v, u or l groove riblets in laminar and turbulent boundary layers, in: *Recent Developments in Turbulence Management*, Springer, 1991, pp. 65–92.
- [13] L. Djenidi, F. Anselmet, J. Liandrat, L. Fulachier, Laminar boundary layer over riblets, *Physics of Fluids* 6 (9) (1994) 2993–2999.
- [14] L. Djenidi, J. Liandrat, F. Anselmet, L. Fulachier, Numerical and experimental investigation of the laminar boundary layer over riblets, *Applied Scientific Research* 46 (3) (1989) 263–270.
- [15] D. Chu, G. Karniadakis, A direct numerical simulation of laminar and turbulent flow over riblet-mounted surfaces, *Journal of Fluid Mechanics* (1993).
- [16] K. Zheng, J. Zhang, H. Dodiuk, S. Kenig, C. Barry, H. Sun, J. Mead, Effect of superhydrophobic composite coatings on drag reduction in laminar flow, *ACS Applied Polymer Materials* 2 (4) (2020) 1614–1622.
- [17] A. Rastegari, R. Akhavan, On drag reduction scaling and sustainability bounds of superhydrophobic surfaces in high reynolds number turbulent flows, *Journal of Fluid Mechanics* 864 (2019) 327–347.
- [18] R. J. Daniello, N. E. Waterhouse, J. P. Rothstein, Drag reduction in turbulent flows over superhydrophobic surfaces, *Physics of Fluids* 21 (8) (2009) 085103.
- [19] W. Barthlott, M. Mail, B. Bhushan, K. Koch, Plant Surfaces: Structures and Functions for Biomimetic Innovations, *Nano-Micro Letters* 9 (2) (2017) 23. doi:10.1007/s40820-016-0125-1.
- [20] H. Teisala, H.-J. Butt, Hierarchical Structures for Superhydrophobic and Superoleophobic Surfaces, *Langmuir* 35 (33) (2019) 10689–10703. doi:10.1021/acs.langmuir.8b03088.
- [21] H. J. Ensikat, P. Ditsche-Kuru, C. Neinhuis, W. Barthlott, Superhydrophobicity in perfection: the outstanding properties of the lotus leaf, *Beilstein Journal of Nanotechnology* 2 (1) (2011) 152–161, publisher: Beilstein-Institut. doi:10.3762/bjnano.2.19.
- [22] Y. Xiang, S. Huang, T.-Y. Huang, A. Dong, D. Cao, H. Li, Y. Xue, P. Lv, H. Duan, Superrepellency of underwater hierarchical structures on *Salvinia* leaf, *Proceedings of the National Academy of Sciences* 117 (5) (2020) 2282–2287. doi:10.1073/pnas.1900015117.
- [23] C. Zhu, X. Yu, J. Lv, J. Zhang, J. Yang, N. Hao, J. Feng, Antisoiling Performance of Lotus Leaf and Other Leaves after Prolonged Outdoor Exposure, *ACS Applied Materials & Interfaces* 12 (47) (2020) 53394–53402. doi:10.1021/acsami.0c13477.
- [24] S. Erramilli, J. Genzer, Influence of surface topography attributes on settlement and adhesion of natural and synthetic species, *Soft Matter* 15 (20) (2019) 4045–4067.
- [25] H. F. Bohn, W. Federle, Insect aquaplaning: *Nepenthes* pitcher plants capture prey with the peristome, a fully wettable water-lubricated anisotropic surface, *Proceedings of the National Academy of Sciences* 101 (39) (2004) 14138–14143. doi:10.1073/pnas.0405885101.
- [26] E. Gorb, Structure and properties of the glandular surface in the digestive zone of the pitcher in the carnivorous plant *Nepenthes ventrata* and its role in insect trapping and retention, *Journal of Experimental Biology* 207 (17) (2004) 2947–2963. doi:10.1242/jeb.01128.
- [27] E. Gorb, V. Kastner, A. Peressadko, E. Arzt, L. Gaume, N. Rowe, S. Gorb, Structure and properties of the glandular surface in the digestive zone of the pitcher in the carnivorous plant *Nepenthes ventrata* and its role in insect trapping and retention, *The Journal of Experimental Biology* (2004) 17.
- [28] U. Bauer, W. Federle, The insect-trapping rim of *Nepenthes* pitchers: surface structure and function, *Plant Signaling & Behavior* 4 (11) (2009) 1019–1023. doi:10.4161/psb.4.11.9664.
- [29] C. Li, C. Yu, S. Zhou, Z. Dong, L. Jiang, Liquid harvesting and transport on multiscaled curvatures, *Proceedings of the National Academy of Sciences* 117 (38) (2020) 23436–23442.
- [30] C. A. Gilman, M. J. Imburgia, M. D. Bartlett, D. R. King, A. J. Crosby, D. J. Irschick, Geckos as springs: Mechanics explain across-species scaling of adhesion, *PLoS One* 10 (9) (2015) e0134604.
- [31] M. J. Imburgia, C.-Y. Kuo, D. R. Briggs, D. J. Irschick, A. J. Crosby, Effects of digit orientation on gecko adhesive force capacity: synthetic and behavioral studies, *Integrative and Comparative Biology* 59 (1) (2019) 182–192.
- [32] D. R. King, M. D. Bartlett, C. A. Gilman, D. J. Irschick, A. J. Crosby, Creating gecko-like adhesives for “real world” surfaces, *Advanced Materials* 26 (25) (2014) 4345–4351.
- [33] S. A. Suresh, A. Hajj-Ahmad, E. W. Hawkes, M. R. Cutkosky, Forcing the issue: testing gecko-inspired adhesives, *Journal of the Royal Society Interface* 18 (174) (2021) 20200730.
- [34] A. B. Croll, N. Hosseini, M. D. Bartlett, Switchable adhesives for multifunctional interfaces, *Advanced Materials Technologies* 4 (8) (2019) 1900193.
- [35] E. Arzt, H. Quan, R. M. McMeeking, R. Hensel, Functional surface microstructures inspired by nature—from adhesion and wetting principles to sustainable new devices, *Progress in Materials Science* 120 (2021) 100823.
- [36] S. Abbott, P. Gaskell, Mass production of bio-inspired structured surfaces, *Proceedings of the Institution of Mechanical Engineers, Part C: Journal of Mechanical Engineering Science* 221 (10) (2007) 1181–1191.
- [37] E. DeGarmo, J. Black, R. Kohser, *Materials and Processes in Manufacturing*, Wiley, 2003.
- [38] R. D. Mehta, Aerodynamics of sports balls, *Annual Review of Fluid Mechanics* 17 (1) (1985) 151–189.
- [39] S. Hong, T. Asai, Aerodynamic effects of dimples on soccer ball surfaces, *Heliyon* 3 (10) (2017) e00432. doi:10.1016/j.heliyon.2017.e00432.
- [40] J. Genzer, J. Groenewold, Soft matter with hard skin: From skin wrinkles to templating and material characterization, *Soft Matter* 2 (4) (2006) 310–323.
- [41] E. P. Chan, A. J. Crosby, Spontaneous formation of stable aligned wrinkling patterns, *Soft Matter* 2 (4) (2006) 324–328.
- [42] S. Raayai-Ardakani, J. Luis Yagüe, K. K. Gleason, M. C. Boyce, Mechanics of graded wrinkling, *Journal of Applied Mechanics* 83 (12) (2016).
- [43] D. Chung, N. Hutchins, M. P. Schultz, K. A. Flack, Predicting the drag of rough surfaces, *Annual Review of Fluid Mechanics* 53 (2021) 439–471.
- [44] D. Bechert, W. Reif, On the drag reduction of the shark skin, *23rd Aerosp Sci Meet* (1985). doi:10.2514/6.1985-546.
- [45] S. Nishimoto, B. Bhushan, Bioinspired self-cleaning surfaces with superhydrophobicity, superoleophobicity, and superhydrophilicity, *Rsc Advances* 3 (3) (2013) 671–690.
- [46] G. D. Bixler, A. Theiss, B. Bhushan, S. C. Lee, Anti-fouling properties of microstructured surfaces bio-inspired by rice leaves and butterfly wings, *Journal of colloid and interface science* 419 (2014) 114–133.
- [47] K. S. Choi, Cost-effective production of microgrooves for drag reduction on the surface of aircraft in situ, *Proc.SPIE* 1573 (1992) 1573 – 9. doi:10.1117/12.57752.
- [48] D. Bechert, G. Hoppe, J. Hoeven, R. Makris, The berlin oil channel for drag reduction research, *Experiments in Fluids* 12-12 (4-5) (1992) 251–260. doi:10.1007/BF00187303.
- [49] S.-J. Lee, S.-H. Lee, Flow field analysis of a turbulent boundary layer over a riblet surface, *Experiments in fluids* 30 (2) (2001) 153–166.
- [50] M. Walsh, L. Weinstein, Drag and heat-transfer characteristics of small longitudinally ribbed surfaces, *AIAA journal* 17 (7) (1979) 770–771.
- [51] B. Launder, S. Li, A numerical study of riblet effects on laminar flow through a plane channel, *Applied Scientific Research* (1989). doi:10.1007/BF00404824.
- [52] Z. Wang, J. Jovanovic, Drag characteristics of extra-thin-fin-riblets in an air flow conduit, *ASME Journal of Fluids Engineering* 115 (2) (1993) 222–226.
- [53] O. El-Samni, H. Chun, H. Yoon, Drag reduction of turbulent flow over thin rectangular riblets, *International Journal of Engineering Science* 45 (2-8) (2007) 436–454.
- [54] D. W. Bechert, M. Bruse, W. Hage, J. Van Der Hoven, G. Hoppe, Experiments on drag-reducing surfaces and their optimization with an adjustable geometry, *Journal of Fluid Mechanics* (1997). doi:10.1017/S0022212096004673.
- [55] S. Raayai-Ardakani, G. H. McKinley, Drag reduction using wrinkled sur-

- faces in high reynolds number laminar boundary layer flows, *Physics of Fluids* 29 (9) (2017) 093605.
- [56] B. Lazos, S. Wilkinson, Turbulent viscous drag reduction with thin-element riblets, *AIAA journal* 26 (4) (1987). doi:10.2514/3.9922.
- [57] D. W. Bechert, M. Bruse, W. Hage, Experiments with three-dimensional riblets as an idealized model of shark skin, *Experiments in Fluids* 28 (5) (2000) 403–412. doi:10.1007/s003480050400.
- [58] S. Grossmann, D. Lohse, C. Sun, High-reynolds number taylor-couette turbulence, *Annual review of fluid mechanics* 48 (2016) 53–80.
- [59] A. Volk, C. J. Kähler, Density model for aqueous glycerol solutions, *Experiments in Fluids* 59 (5) (2018) 1–4.
- [60] D. P. Lathrop, J. Fineberg, H. L. Swinney, Transition to shear-driven turbulence in couette-taylor flow, *Physical Review A* 46 (10) (1992) 6390.
- [61] D. P. Lathrop, J. Fineberg, H. L. Swinney, Turbulent flow between concentric rotating cylinders at large reynolds number, *Physical review letters* 68 (10) (1992) 1515.
- [62] J. F. Thompson, F. C. Thames, C. W. Mastin, Automatic numerical generation of body-fitted curvilinear coordinate system for field containing any number of arbitrary two-dimensional bodies, *Journal of computational physics* 15 (3) (1974) 299–319.
- [63] C. Varier, 2D-Elliptic-Mesh-Generator, <https://github.com/cvarier/2D-Elliptic-Mesh-Generator>, [Online; accessed 15-January-2022] (2017).
- [64] P. Vukoslavcevic, J. Wallace, J.-L. Balint, Viscous drag reduction using streamwise-aligned riblets, *AIAA journal* 30 (4) (1992) 1119–1122.
- [65] A. G. Domel, G. Domel, J. C. Weaver, M. Saadat, K. Bertoldi, G. V. Lauder, Hydrodynamic properties of biomimetic shark skin: effect of denticle size and swimming speed, *Bioinspiration & biomimetics* 13 (5) (2018) 056014.